Interfacial charge-transfer Mott state in iridate–nickelate superlattices

Xiaoran Liu[a,1], Michele Kotiuga[a], Heung-Sik Kim[a], Alpha T. N'Diaye[b], Yongseong Choi[c], Qinghua Zhang[d], Yanwei Cao[e], Mikhail Kareev[a], Fangdi Wen[a], Banabir Pal[a], John W. Freeland[c], Lin Gu[d], Daniel Haskel[c], Padraic Shafer[b], Elke Arenholz[b,2], Kristjan Haule[a], David Vanderbilt[a], Karin M. Rabe[a,1], and Jak Chakhalian[a]

[a]Department of Physics and Astronomy, Rutgers University, Piscataway, NJ 08854; [b]Advanced Light Source, Lawrence Berkeley National Laboratory, Berkeley, CA 94720; [c]Advanced Photon Source, Argonne National Laboratory, Argonne, IL 60439; [d]Beijing National Laboratory for Condensed-Matter Physics and Institute of Physics, Chinese Academy of Sciences, Beijing 100190, China; and [e]Ningbo Institute of Materials Technology and Engineering, Chinese Academy of Sciences, Ningbo, Zhejiang 315201, China

Contributed by Karin M. Rabe, August 16, 2019 (sent for review May 6, 2019; reviewed by Ivan Bozovic and Claude Ederer)

We investigate $SrIrO_3$/$LaNiO_3$ superlattices in which we observe a full electron transfer at the interface from Ir to Ni, triggering a massive structural and electronic reconstruction. Through experimental characterization and first-principles calculations, we determine that a large crystal field splitting from the distorted interfacial IrO_6 octahedra surprisingly dominates over the spin–orbit coupling and together with the Hund's coupling results in the high-spin (S = 1) configurations on both the Ir and Ni sites. This demonstrates the power of interfacial charge transfer in coupling lattice, charge, orbital, and spin degrees of freedom, opening fresh avenues of investigation of quantum states in oxide superlattices.

superlattice | interfacial charge transfer | iridates | nickelates

The ability to construct heterostructures layer by layer provides the opportunity to combine multiple materials with different properties and generate emergent quantum states quite distinct from the individual components (1). One key factor in novel heterostructure physics is the presence of interfaces with electronic and structural reconstructions. In particular, interfacial charge transfer (ICT), well known to occur in conventional semiconductor/metal heterojunctions due to work function mismatch, can lead to exotic scenarios in complex oxide heterostructures (2). The transferred charge can couple to the lattice, orbital, and/or spin degrees of freedom, modifying the structural, electronic, and magnetic properties of constituent materials at the interface (2–5).

While most previous studies of ICT in complex oxides have focused on heterostructures incorporating $3d$ and $4d$ transition metal oxides (6), the $5d$ iridates are uniquely positioned to host a variety of interesting quantum phases as their strong spin–orbit coupling (SOC), on the order of ∼0.5 eV, is comparable to the on-site Coulomb repulsion, U, and crystal-field (CF) splitting Δ_{CF} (7–12). $SrIrO_3$ is an exotic semimetal due to its strong SOC (13, 14). However, ICT does not occur in most artificial heterostructures and superlattices involving iridates studied to date, such as $SrIrO_3$/$SrTiO_3$ and $SrIrO_3$/$SrRuO_3$ systems (15–22).

In oxide heterostructures a simple potential energy argument in which the O $2p$ bands are aligned at the interface has proved effective in predicting whether charge transfer between d states will occur (23, 24) and furthermore explains the absence of ICT in the aforementioned iridate systems. Recently, ICT has been observed in $SrIrO_3$/$SrMnO_3$ systems (25–27). One can explain the ICT from the simple potential energy argument: The Ir $5d$ and O $2p$ orbitals have a large on-site energy difference (∼1 eV) whereas such an on-site energy difference is not present in $SrMnO_3$ (28).

ICT has been observed in a number of heterostructures with $LaNiO_3$, such as the $LaTiO_3$/$LaNiO_3$ interface (23, 29–31). As in all rare-earth nickelates (32), the O $2p$ orbitals of $LaNiO_3$ are hybridized with the Ni $3d$ orbitals and span the Fermi energy, making $LaNiO_3$ an ideal material to act as an electron acceptor in this potential energy scheme.

Following this reasoning, a large interfacial electron transfer from the Ir $5d$ orbital to the Ni $3d$ orbital is anticipated in the $SrIrO_3$/$LaNiO_3$ superlattices (Fig. 1). SOC effects in the resulting Ir^{5+} (d^4) would imply a nonmagnetic state (11); however, recent work has revealed the possibility of a magnetic state due to the competition of SOC with Hund's coupling and structural effects (33, 34). This ICT and ultrathin superlattice geometry thus level the playing field, giving us the opportunity to investigate the interplay of SOC, Hund's coupling, and crystal-field effects in systems containing Ir^{5+}, leading to exotic quantum states.

In this article, we present experimental and theoretical results on a set of $SrIrO_3$/$LaNiO_3$ superlattices designed specifically to address those issues. Strikingly, we find from X-ray absorption spectroscopy (XAS) and first-principles calculations the signature of a transfer from Ir to Ni of close to one electron per lateral unit cell, switching the electronic configurations from $5d^5/3d^7$ to $5d^4/3d^8$, in tandem with a structural change observed in our

Significance

Heterojunctions between dissimilar materials provide an opportunity to generate emergent properties not present in their individual components. These properties are often linked to interfacial charge transfer, an important mechanism allowing one to access and control novel quantum states. Here, we have grown unit-cell scale superlattices composed of 5*d* $SrIrO_3$ and 3*d* $LaNiO_3$. We have discovered a massive interfacial charge transfer from Ir to Ni, triggering dramatic electronic and magnetic reconstructions at the interface that suppress strong spin–orbit coupling effects normally present in the iridates. These findings call for careful evaluation and reinterpretation of experiments on spin–orbit-driven physics in thin films and heterostructures based on prototypical 5*d* transition metal oxides.

Author contributions: X.L. and J.C. designed research; X.L., A.T.N., Y. Choi, Q.Z., Y. Cao, M. Kareev, F.W., B.P., J.W.F., L.G., D.H., P.S., and E.A. performed experiments; M. Kotiuga, H.-S.K., K.H., D.V., and K.M.R. performed calculations; X.L., M. Kotiuga, A.T.N., and Y. Choi analyzed data; X.L., M. Kotiuga, K.M.R., and J.C. wrote the paper.

Reviewers: I.B., Brookhaven National Laboratory (US Department of Energy); and C.E., ETH Zurich.

The authors declare no conflict of interest.

Published under the PNAS license.

[1]To whom correspondence may be addressed. Email: xiaoran.liu@rutgers.edu or kmrabe@physics.rutgers.edu.

[2]Present address: Cornell High Energy Synchrotron Source, Cornell University, Ithaca, NY 14853.

This article contains supporting information online at www.pnas.org/lookup/suppl/doi:10.1073/pnas.1907043116/-/DCSupplemental.

First published September 16, 2019.

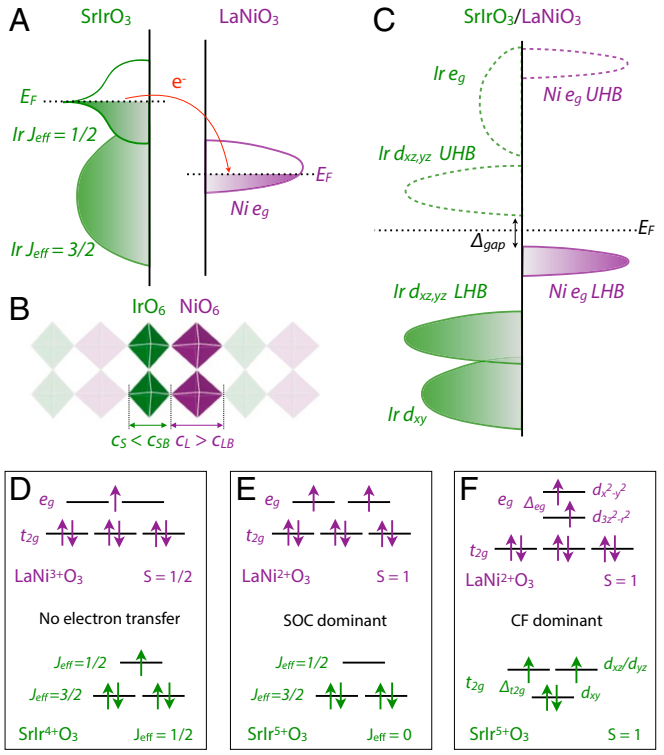

Fig. 1. (*A*) Schematic densities of states of bulk $SrIrO_3$ and $LaNiO_3$. (*B*) Schematic structure of the representative 1I/1N superlattice. Note the compression of IrO_6 and elongation of NiO_6 octahedra are described by comparing their out-of-plane height to the bulk as $c_S < c_{SB}$, $c_L > c_{LB}$. (*C*) Schematic density of state of the 1I/1N superlattice. (*D*–*F*) Schematic energy-level diagrams and orbital splitting configurations of Ni and Ir in (*D*) bulk, (*E*) $SrIrO_3$/$LaNiO_3$ interface with SOC dominant, and (*F*) $SrIrO_3$/$LaNiO_3$ interface with CF dominant.

first-principles calculations and X-ray linear dichroism (XLD) measurements. X-ray magnetic circular dichroism (XMCD) measurements and first-principles results demonstrate that these electronic and structural changes drive $SrIrO_3$ from the strong SOC state to a Mott state stabilized by the crystal field splitting with $S = 1$ high-spin configurations on both the Ni and Ir sites. These findings demonstrate how, by virtue of interface engineering, the interplay between ICT, electron correlation, SOC, and lattice degrees of freedom gives rise to unusual quantum states.

A series of $[(SrIrO_3)_m/(LaNiO_3)_n]_N$ superlattices ("$[m\mathrm{I}/n\mathrm{N}]_N$": Here m and n refer to the number of $SrIrO_3$ and $LaNiO_3$ pseudocubic unit cells, respectively) are epitaxially grown on (001) $SrTiO_3$ substrates by pulsed laser deposition (PLD), starting with $LaNiO_3$ and terminated by $SrIrO_3$ layers. We grew and experimentally characterized the 1I/1N, 1I/3N, 2I/3N, 4I/3N, and 1I/10N superlattices. While the interfaces are polar, the layers in our systems are too thin for a polarization catastrophe to occur, except for the 1I/10N superlattice, in which the $LaNiO_3$ layer is metallic (35). As the $SrTiO_3$ substrates are not chemically treated, we did not specifically control the termination of each layer, and the interface termination in PLD growth is likely a mixture of both IrO_2-SrO-NiO_2-LaO and SrO-IrO_2-LaO-NiO_2 cases. The periodicity N is selected to keep the total thickness of each superlattice between 15 and 20 nm. Complementary atomic-scale information about atomic arrangement and electronic states at the interface is obtained from first-principles density-functional theory (DFT) calculations for the 1I/1N superlattice to focus on the interfacial effects.

Results and Discussion

We begin our experimental characterization of the ICT using element-specific XAS measurements (Fig. 2 *A* and *B*). For each superlattice, the Ni L_2 edge shows a mixture of both Ni^{2+} and Ni^{3+} features and the peak position of the Ir L_3 edge shifts toward higher energy with respect to the reference peak of Ir^{4+}, indicating the Ir oxidation state increases (39). These combined results clearly demonstrate that electrons are intrinsically transferred from Ir to Ni sites, giving rise to hole(electron)-doped $SrIrO_3$ ($LaNiO_3$) layers, respectively. We estimate the average oxidation state of Ir by calculating the relative peak shift with respect to the positions of nominal Ir^{4+} and Ir^{5+} reference materials (39) and of Ni by spectral deconvolution of Ni L_2 XAS (*SI Appendix*, Fig. S4). For the 1I/nN series (Fig. 2*C*), we observe that the average Ir oxidation state remains almost constant at Ir^{5+}, indicating that the single-unit-cell $SrIrO_3$ layer is hole doped at about 1 hole per Ir. The Ni oxidation state at $n = 1$ is significantly reduced from the nominal Ni^{3+} to $Ni^{2.2+}$, indicating that the single-unit-cell $LaNiO_3$ layer is electron doped at about 1 electron per Ni. As n increases, the average Ni oxidation state approaches the nominal valence, consistent with a net transfer of 1 electron from the single-unit-cell $SrIrO_3$ layer, independent of n. For the mI/3N series (Fig. 2*D*), the average Ir oxidation state increases from $Ir^{4.3+}$ ($m = 4$) to $Ir^{4.9+}$ ($m = 1$) with decreasing m, whereas the average Ni

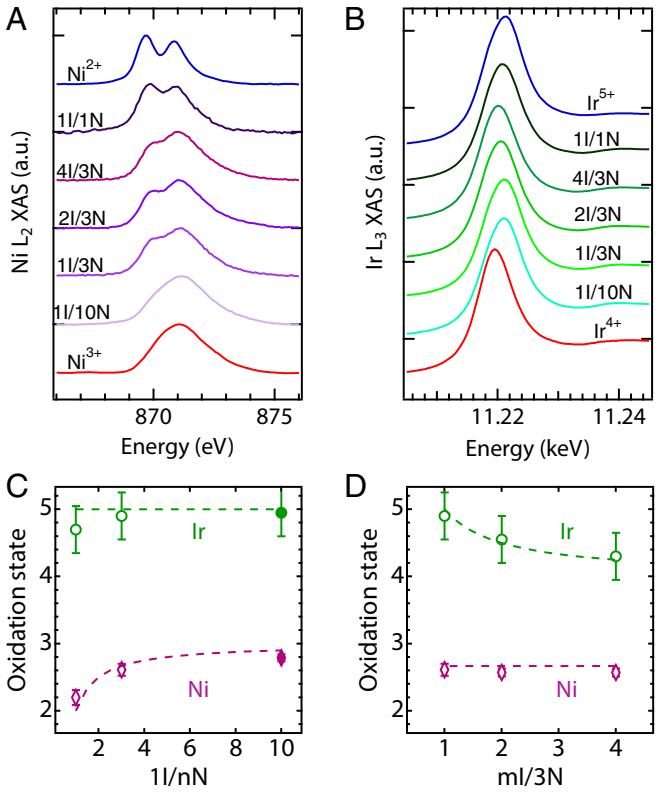

Fig. 2. (*A* and *B*) Resonant XAS near (*A*) the Ni L_2 edge at 20 K and (*B*) the Ir L_3 edge at 5 K, respectively. The blue and red curves are adapted from the literature as representative spectra of Ni^{2+} from Ca_2OsNiO_6 (36), Ni^{3+} from $LaNiO_3$ (37), Ir^{4+} from $SrIrO_3$ (38), and Ir^{5+} from Sr_2IrFeO_6 (39). (*C* and *D*) Average oxidation state of each cation in the superlattices classified into 2 series: 1I/nN (n = 1, 3, 10) and mI/3N (m = 1, 2, 4). All superlattices are insulating (open circles), as might be expected from the ultralow thickness of the constituent layers, except for 1I/10N, which is metallic (solid circles); for transport data see *SI Appendix*, Fig. S3. The dashed curves show the average oxidation states computed assuming a net transfer of 1 electron per lateral unit cell from the $SrIrO_3$ layer to the $LaNiO_3$ layer.

oxidation state remains constant at approximately $Ni^{2.6+}$. Using a simple model assuming a net transfer of 1 electron per lateral unit cell from the m-unit-cell $SrIrO_3$ layer to the n-unit-cell $LaNiO_3$ layer, we find good agreement with the experimental results (dashed lines in Fig. 2 *C* and *D*). In this model, the average oxidation state of Ni is given by $3-1/n$ and the average oxidation state of Ir is given by $4+1/m$. If the transferred electron and hole are taken each to selectively localize on a single ion, which in general will involve symmetry breaking, this results in integer values in an unusual configuration: $Ir^{4+}/Ni^{3+} \rightarrow Ir^{5+}/Ni^{2+}$.

To quantify the effect of such a massive ICT on the orbital splitting and spin states, we probe the occupation of Ni e_g orbitals by XLD. As sketched in Fig. 3*A*, this approach uses X-rays with different linear polarizations (i.e., in-plane $E \parallel ab$ vs. out-of-plane $E \parallel c$), which can selectively probe the valence holes on orbitals with different orientations, in our case $d_{x^2-y^2}$ vs. $d_{3z^2-r^2}$. The difference of these 2 spectra gives rise to the XLD signal, I_c - I_{ab}. As shown in Fig. 3*B*, a representative spectrum of the 1I/1N superlattice recorded with in-plane polarization (blue curve) shifts ~0.2 eV higher in energy with respect to that with out-of-plane polarization (red curve), showing that the energy of the Ni $d_{x^2-y^2}$ orbital is higher than that of the $d_{3z^2-r^2}$ orbital with a splitting $\Delta_{e_g} \simeq 0.2$ eV (29). Such splitting can directly result from a symmetry-breaking distortion of the oxygen octahedron around the Ni (40, 41). The origin of this distortion is not the tensile epitaxial strain in the $LaNiO_3$ layer; while epitaxial strain does deform the octahedra and splits the e_g levels in $LaNiO_3$, the splitting for $LaNiO_3$ films under tensile strain is reported to be close to 0 (37) or to have the opposite sign (42, 43). Furthermore, the integrated value of the 1I/1N XLD intensity is close to 0, indicating that both orbitals are almost equally occupied (42), consistent with a transferred electron yielding high-spin ($S = 1$) Ni^{2+}, favored by Hund's coupling. We therefore attribute the observed splitting to the deformation of $Ir^{5+}O_6$ and $Ni^{2+}O_6$ octahedra caused by the ICT, leading to a significant noncubic CF splitting with elongated NiO_6 octahedra (Fig. 1*F*). This is further supported by the result shown in Fig. 3*C* that the XLD signal diminishes in intensity, indicating a smaller splitting, as n increases and the proportion of $Ni^{2+}O_6$ octahedra decreases.

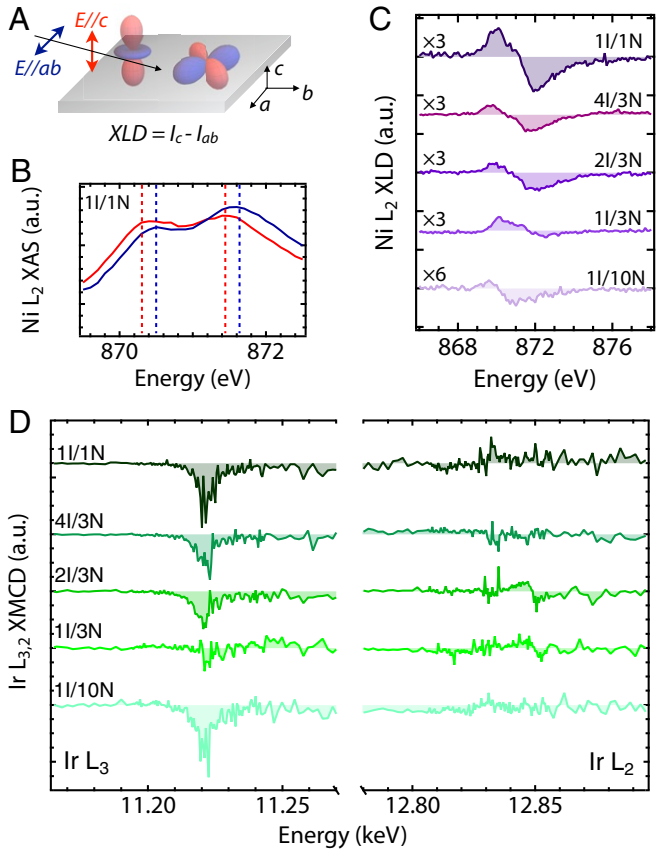

Fig. 3. (*A*) Schematic of XLD setup. (*B*) Magnified Ni L_2 XAS of the 1I/1N superlattice. The red and blue dashed lines refer to the peak positions of spectra taken with out-of-plane ($E \parallel c$) and in-plane ($E \parallel ab$) polarizations. (*C*) Ni L_2 XLD at 300 K. (*D*) Ir $L_{2,3}$ XMCD at 5 K under H = 4 T.

To investigate the magnetism of iridium, we measure the XAS near the Ir $L_{2,3}$ edges using both left- and right- polarized X-rays. The spectral difference, known as the XMCD, is sensitive to the net magnetic moments of the ions. Specifically, a nonmagnetic system would have no XMCD signal, a ferromagnetic system would exhibit a large signal, and an antiferromagnetic or paramagnetic system would exhibit a small signal in an applied magnetic field. As displayed in Fig. 3*D*, all samples exhibit a negative signal at the Ir L_3 edge that is modest compared to bulk Sr_2IrO_4 (44) and a markedly smaller signal with no clear sign at the Ir L_2 edge. We note that such XMCD behavior is very different from the results of iridate–manganite systems, in which ICT is also observed, which typically show comparable intensities at the Ir $L_{2,3}$ edges with the same sign due to the dominance of the contribution from the orbital moments (19, 25, 27). Branching ratio (BR) and sum rules analyses (*SI Appendix*, Fig. S6 and Table S2) are applied to investigate the strength of SOC of all samples, as summarized in Table 1. The presence of SOC is evident from the BR falling into the range of 5.0 to 5.5 (7, 39). However, the ratio of orbital moment to spin moment is small ($M_O/M_S \leq 0.7$, being lowest for 1I/1N) compared to that of iridate-based systems in the strong SOC limit ($M_O/M_S \geq 2.0$) (19, 45, 46). The nonzero but small value of M_{Ir} suggests that the magnetic ordering of Ir moments in the superlattices may be either paramagnetic or canted antiferromagnetic.

With this information, we can determine which density-of-states scenario (Fig. 1 *E* or *F*) is realized in these superlattices. As the XMCD results clearly demonstrate the existence of a local moment on Ir, the system cannot be in the strong SOC limit, as one would then expect a nonmagnetic $J_{eff} = 0$ ground state (Fig. 1*E*). Furthermore, as our XLD results suggest elongated interfacial NiO_6 octahedra, we expect the adjacent IrO_6 octahedra to be compressed, removing the t_{2g} degeneracy by lowering the d_{xy} orbital. In fact, it has been recently shown that the validity of the strong SOC limit critically depends on the degree of IrO_6 octahedral distortions which can induce a noncubic CF splitting of comparable strength (33, 34), causing strong mixing of the $J_{eff} = 1/2$ and $J_{eff} = 3/2$ states. As a result, the SOC no longer dominates the level structure of the Ir t_{2g} orbitals and, instead, the CF energy scale dominates the electronic structure (Fig. 1*F*). This scenario is consistent with all our experimental observations.

To further elucidate the microscopic details of the $SrIrO_3$/$LaNiO_3$ interface and the associated electronic reconstruction, we carried out first-principles calculations. As the films are coherently strained to $SrTiO_3$, we constrain the in-plane lattice constants (a and b) while allowing the c axis to relax for a variety of starting tilt patterns. The lowest-energy structure found has Pc symmetry and $c = 8.13$ Å, with a tilt pattern derived from $a^-a^-c^-$, where the tilt angles around the c axis are different in the Ni and Ir layers, consistent with our experimental observation (*SI Appendix*, Fig. S2). The computed c axis of the $LaNiO_3$ layer (4.22 Å) is elongated relative to $LaNiO_3$ under tensile strain on $SrTiO_3$ (3.76 Å) and the c axis of the

Table 1. Summary of BR and sum rule analysis of the XMCD results

*m*l/*n*N	BR	$\langle L \cdot S \rangle$, $\hbar^2$	M_{Ir}, μ_B	M_O/M_S
4/3	5.3	2.8	0.04	0.7
2/3	5.4	2.9	0.04	0.6
1/3	5.3	3.1	0.01	0.4
1/1	5.5	3.1	0.06	0.4
1/10	5.1	3.0	0.05	0.7

M_{Ir}, M_O, and M_S represent the net magnetic moment of Ir, its orbital magnetic moment, and its spin magnetic moment, respectively.

$SrIrO_3$ layer (3.91 Å) is compressed relative to $SrIrO_3$ under compressive strain on $SrTiO_3$ (4.05 Å). The NiO_6 octahedra are elongated along one axis and have a volume of 11.4 $Å^3$, about 13% larger than in $LaNiO_3$ on $SrTiO_3$, similar to electron-doped $SmNiO_3$ (47, 48). The IrO_6 octahedra have a volume of 10.9 $Å^3$, about 4% smaller than $SrIrO_3$ on $SrTiO_3$, and are compressed along one axis of the octahedra. It is the electron transfer that leads to the substantial difference from the strained bulk values and leads to a net overall volume increase of the system relative to the average of the constituent compound volumes. We conjecture that such a deformation of octahedra at the interface is due to the cooperative effects of the NiO_6 octahedra expansion within the epitaxial constraint and the Madelung energy response to the charge modulation. The latter is described by a simple ionic model (49) in which the charge transfer leads the formation of $Ni^{2+}O_2$ and $Ir^{5+}O_2$ planes, with net charge -2 and $+1$, respectively. The apical O^{2-} ions tend to shift away from the negatively charged NiO_2 planes and toward the positively charged IrO_2 planes. As a consequence, the NiO_6 octahedra are elongated while the adjacent IrO_6 octahedra are compressed.

We find the relative energies of the Ir and Ni orbitals, consistent with Fig. 1*F*, to be intimately linked with the octahedral compression and elongation, respectively, and the associated crystal-field splitting. Ni has a local magnetic moment of 1.6 μ_B indicating a high-spin ($S = 1$) Ni^{2+} state and Ir has a magnetic moment of 0.8 μ_B indicating an orbital splitting dictated by the crystal-field splitting, noting that SOC alone would result in a nonmagnetic $J_{\text{eff}} = 0$ state. The magnetic ordering in the Ni layers is checkerboard-type antiferromagnetic (AFM), with moments directed along the c axis. In the Ir layers, the moments lie in the ab plane with a checkerboard ordering where the moments have an $\sim 150^\circ$ angle to one another, resulting in an in-plane ferrimagnetic ordering. Doubling the supercell along the c axis, we find that the magnetic orderings within the Ni and Ir layers remain the same and various relative alignments from layer to layer result in the same energy to within 0.3 meV per magnetic ion. This negligible interplane coupling implies that the system is not ferromagnetic and suggests the smallness of the XMCD signal arises from an AFM interlayer ordering of the Ir layers or a paramagnetic ordering (see *SI Appendix*, Table S3 for moment components).

The results for the band structure and the Ir and Ni d-orbital projected density of states (displayed in Fig. 4) show a semimetallic state with a very small overlap between the Ni-dominated valence band (purple) and the Ir-dominated conduction band (green). This overlap can be attributed to the approximate treatment of correlation effects in DFT, which often underestimates the band gap. The top of the valence band, with Ni $d_{x^2-y^2}$ character, is composed of the states into which the electron has been transferred. The remaining occupied Ni states (t_{2g} and $d_{3r^2-z^2}$ orbitals) are lower in energy, consistent with the crystal-field splitting of an octahedron elongated along the z axis. The unoccupied Ni e_g orbitals are well above the conduction band minimum (*SI Appendix*, Fig. S7). The conduction band minimum is associated with the hole left from the transferred electron and is composed of the Ir $d_{xz,yz}$ orbitals, while the remaining Ir t_{2g} orbitals are occupied and are positioned well below the valence band, with the unoccupied Ir e_g orbitals above the conduction band minimum. We comment that first-principles calculation for FM ordering within the Ni layers shows dispersive $d_{x^2-y^2}$ bands which lead to metallic character (*SI Appendix*, Fig. S8). Overall we find that the transferred electron localizes on Ni, leading to an $S = 1$ state due to its large Hund's coupling. The NiO_6 octahedra elongate along the c axis as a result of electron doping and the in-plane constraint, compressing the IrO_6 octahedra. This stabilizes an $S = 1$ Ir state, where the large low-symmetry crystal-field splitting dominates the spin–orbit coupling.

Going forward, first-principles calculations of the electronic structure for longer-period superlattices (m and/or $n > 1$) could address a number of interesting open questions. With 1 electron per lateral unit cell transferred from the $SrIrO_3$ layer to the $LaNiO_3$ layer, as indicated by the XAS results, charge-ordered layers are expected in the longer-period superlattices, which could couple to local structural distortions and electronic states at the interface. Investigation of the transport properties for thicker layers, including charge ordering, could explain the underlying mechanism of the insulating nature of the short-period superlattices experimentally characterized and suggest additional experimental characterization.

Conclusions

In summary, we have experimentally realized a series of high-quality iridate–nickelate superlattices. We observe up to a full electron transfer at the $SrIrO_3/LaNiO_3$ interface from the Ir to the Ni site, triggering a dramatic electronic and magnetic reconstruction. Unlike the vast majority of iridates where the strong SOC dominates and thus defines the ground state, here the interface-driven octahedral distortions induce a large crystal-field splitting leading to the breakdown of the SOC picture. An unusual $S = 1$ magnetic state emerges for the Ir^{5+} ions in the superlattices. The experimental findings are well supported by the first-principles calculations, which reveal the Mott

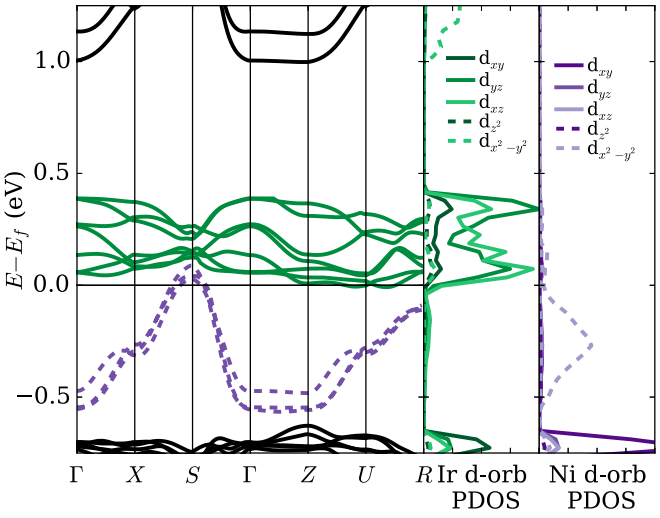

Fig. 4. Calculated band structures for the antiferromagnetic 1I/1N superlattice using DFT+*U* with SOC included. The solid green conduction bands are dominated by Ir $d_{xz,yz}$ states where the electron was transferred from. The dashed purple valence bands are dominated by Ni $d_{x^2-y^2}$ states where the electron is transferred to. The projected densities of states (PDOS) of the *d* orbitals for Ir and Ni are shown at *Right*.

character of the band gap, determined collectively by Ir and Ni Hubbard subbands. Our findings push past the idea of "band bending" (50) for ICT systems to a regime of "band reorganization" and highlight the need for careful evaluation and possible reinterpretation of the spin–orbit-driven physics in ultrathin films and heterostructures based on $5d$ transition metal oxides.

Materials and Methods

Superlattice Growth. All superlattices were deposited on a (001) $SrTiO_3$ substrate. Sintered Sr_2IrO_4 and $LaNiO_3$ targets were alternately ablated by a KrF excimer laser (λ = 248 nm, fluence $\sim$2 J·cm^{-2}) at 2 Hz and 10 Hz, respectively (38, 51). A substrate temperature of 650 °C and an oxygen partial pressure of 50 mTorr were maintained during deposition. After growth the samples were cooled down to room temperature in 1 atm of pure oxygen. Combined in situ reflection high-energy electron diffraction, X-ray diffraction, scanning transmission electron microscopy, and reciprocal space mapping confirm the high crystallinity of the coherently strained samples with abrupt interfaces, as well as the expected thickness and periodicity (*SI Appendix*, Fig. S1).

Polarized X-Ray Absorption Spectra. Resonant XAS and XLD measurements near Ni $L_{2,3}$ edges were taken in the luminescence yield detection mode at beamlines 6.3.1 and 4.0.2 of the Advanced Light Source (ALS), Lawrence Berkeley National Laboratory. The X-rays were incident at an angle of 20° relative to the film surface. Resonant XMCD spectra near Ir $L_{2,3}$ edges were taken in the fluorescence yield mode at beamline 4IDD of the Advanced Photon Source (APS), Argonne National Laboratory. The X-rays were incident at an angle of 3° relative to the film surface. Data were taken in both +4 T and −4 T magnetic fields to eliminate experimental artifacts.

First-Principles Calculation. First-principles DFT calculations were carried out on the 1I/1N superlattice using VASP (52), using the Perdew–Burke–Ernzerhof (PBE) exchange-correlation potential (53, 54) along with projector augmented wave (PAW) potentials (55, 56). A Hubbard U [within the rotationally invariant method of Liechtenstein et al. (57)] was included using U_{Ni} = 4.6, U_{Ir} = 2.6, $J_{Ni} = J_{Ir}$ = 0.6. We use a 2×2×2 supercell, relative to the 5-atom perovskite primitive cell, with 4 B sites in each layer. To satisfy the epitaxial constraint, the in-plane lattice parameter is fixed to that of $SrTiO_3$ with a = 3.94 Å, the calculated lattice parameter of $SrTiO_3$ with DFT-PBE. This follows standard practice for first-principles calculations of the effects of epitaxial strain, which is based on the assumption that the relative lattice parameters for the compounds of interest are correct despite the known discrepancies of the absolute numbers from the experimental values. The out-of-plane lattice parameter is relaxed along with the internal coordinates to a tolerance of 0.005 eV/Å. The density-of-states calculations used the tetrahedral method with Blöchl corrections (58) and included spin–orbit coupling.

ACKNOWLEDGMENTS. We gratefully acknowledge experimental assistance from X. Li, J.-S. Zhou, and E. Karapetrova. X.L. and J.C. were supported by the Gordon and Betty Moore Foundation's Emergent Phenomena in Quantum Systems Initiative (EPiQS) Initiative through Grant GBMF4534 and by the Department of Energy (DOE) under Grant DE-SC0012375. M. Kotiuga and K.M.R. acknowledge support from Office of Naval Research Grant N000014-17-1-2770, National Science Foundation (NSF) Grant DMR-1629346, and the Department of Defense High Performance Computing Modernization Program for computational resources. H.-S.K. and K.H. were supported by NSF Grant DMREF DMR-1629059. D.V. acknowledges support from Office of Naval Research Grant N00014-16-1-2951. This research used resources of the Advanced Light Source, which is a DOE Office of Science User Facility under Contract DE-AC02-05CH11231. This research used resources of the Advanced Photon Source, a US DOE Office of Science User Facility operated by Argonne National Laboratory under Contract DE-AC02-06CH11357.

1. H. Y. Hwang *et al.*, Emergent phenomena at oxide interfaces. *Nat. Mater.* **11**, 103–113 (2012).
2. J. Chakhalian *et al.*, Colloquium: Emergent properties in plane view: Strong correlations at oxide interfaces. *Rev. Mod. Phys.* **86**, 1189–1202 (2014).
3. P. Zubko, S. Gariglio, M. Gabay, P. Ghosez, J.-M. Triscone, Interface physics in complex oxide heterostructures. *Annu. Rev. Condens. Matter Phys.* **2**, 141–165 (2011).
4. J. Mannhart, D. G. Schlom, Oxide interfaces–an opportunity for electronics. *Science* **327**, 1607–1611 (2010).
5. S. Stemmer, S. J. Allen, Two-dimensional electron gases at complex oxide interfaces. *Annu. Rev. Mater. Res.* **44**, 151–171 (2014).
6. H. Chen, A. Millis, Charge transfer driven emergent phenomena in oxide heterostructures. *J. Phys. Condens. Matter* **29**, 243001 (2017).
7. B. J. Kim *et al.*, Novel J_{eff} = 1/2 Mott state induced by relativistic spin-orbit coupling in Sr_2IrO_4. *Phys. Rev. Lett.* **101**, 076402 (2008).
8. B. J. Kim *et al.*, Phase-sensitive observation of a spin-orbital Mott state in Sr_2IrO_4. *Science* **323**, 1329–1332 (2009).
9. S. J. Moon *et al.*, Dimensionality-controlled insulator-metal transition and correlated metallic state in 5*d* transition metal oxides $Sr_{n+1}Ir_nO_{3n+1}$ (n = 1, 2, and ∞). *Phys. Rev. Lett.* **101**, 226402 (2008).
10. W. Witczak-Krempa *et al.*, Correlated quantum phenomena in the strong spin-orbit regime. *Annu. Rev. Condens. Matter Phys.* **5**, 57–82 (2014).
11. J. G. Rau, E. K. Lee, H. Kee, Spin-orbit physics giving rise to novel phases in correlated systems: Iridates and related materials. *Annu. Rev. Condens. Matter Phys.* **7**, 195–221 (2015).
12. R. Schaffer *et al.*, Recent progress on correlated electron systems with strong spin-orbit coupling. *Rep. Prog. Phys.* **79**, 094504 (2016).
13. M. A. Zeb, H.-Y. Kee, Interplay between spin-orbit coupling and Hubbard interaction in $SrIrO_3$ and related *Pbnm* perovskite oxides. *Phys. Rev. B* **86**, 085149 (2012).
14. Y. F. Nie *et al.*, Interplay of spin-orbit interactions, dimensionality, and octahedral rotations in semimetallic $SrIrO_3$. *Phys. Rev. Lett.* **114**, 016401 (2015).
15. I. Fina *et al.*, Anisotropic magnetoresistance in an antiferromagnetic semiconductor. *Nat. Commun.* **5**, 4671 (2014).
16. J. Matsuno *et al.*, Engineering a spin-orbital magnetic insulator by tailoring superlattices. *Phys. Rev. Lett.* **114**, 247209 (2015).
17. D. J. Groenendijk *et al.*, Epitaxial growth and thermodynamic stability of $SrIrO_3/SrTiO_3$ heterostructures. *Appl. Phys. Lett.* **109**, 041906 (2016).
18. D. Hirai. J. Matsuno, H. Takagi, Fabrication of (111)-oriented $Ca_{0.5}Sr_{0.5}IrO_3/SrTiO_3$ superlattices – A designed playground for honeycomb physics. *Appl. Mater.* **3**, 041508 (2015).
19. D. Yi *et al.*, Atomic-scale control of magnetic anisotropy via novel spin-orbit coupling effect in $La_{2/3}Sr_{1/3}MnO_3/SrIrO_3$ superlattices. *Proc. Natl. Acad. Sci. U.S.A.* **113**, 6397–6402 (2016).
20. J. Matsuno *et al.*, Interface-driven topological Hall effect in $SrRuO_3 - SrIrO_3$ bilayer. *Sci. Adv.* **2**, e1600304 (2016).
21. J. H. Gruenewald *et al.*, Engineering 1D quantum stripes from superlattices of 2D layered materials. *Adv. Mater.* **29**, 1603798 (2017).
22. L. Hao *et al.*, Two-dimensional J_{eff} = 1/2 antiferromagnetic insulator unraveled from interlayer exchange coupling in artificial perovskite iridate superlattices. *Phys. Rev. Lett.* **119**, 027204 (2017).
23. H. Chen, A. J. Millis, C. M. Marianetti, Engineering correlation effects via artificially designed oxide superlattices. *Phys. Rev. Lett.* **111**, 116403 (2013).
24. Z. Zhong, P. Hansmann, Band alignment and charge transfer in complex oxide interfaces. *Phys. Rev. X* **7**, 011023 (2017).
25. J. Nichols *et al.*, Emerging magnetism and anomalous Hall effect in iridate–manganite heterostructures. *Nat. Commun.* **7**, 12721 (2016).
26. S. Okamoto *et al.*, Charge transfer in iridate–manganite superlattices. *Nano Lett.* **17**, 2126–2130 (2017).
27. D. Yi *et al.*, Tuning perpendicular magnetic anisotropy by oxygen octahedral rotations in $(La_{1-x}Sr_xMnO_3)/(SrIrO_3)$ superlattices. *Phys. Rev. Lett.* **119**, 077201 (2017).
28. H. Chen, H. Park, A. J. Millis, C. M. Marianetti, Charge transfer across transition-metal oxide interfaces: Emergent conductance and electronic structure. *Phys. Rev. B* **90**, 245138 (2014).
29. Y. Cao *et al.*, Engineered Mott ground state in a $LaTiO_{3+\delta}/LaNiO_3$ heterostructure. *Nat. Commun.* **7**, 10418 (2016).
30. H. Chen *et al.*, Modifying the electronic orbitals of nickelate heterostructures via structural distortions. *Phys. Rev. Lett.* **110**, 186402 (2013).
31. A. S. Disa *et al.*, Orbital engineering in symmetry-breaking polar heterostructures. *Phys. Rev. Lett.* **114**, 026801 (2015).
32. S. Catalano *et al.*, Rare-earth nickelates $RNiO_3$: Thin films and heterostructures. *Rep. Prog. Phys.* **81**, 046501 (2018).
33. X. Liu *et al.*, Testing the validity of the strong spin-orbit-coupling limit for octahedrally coordinated iridate compounds in a model system Sr_3CuIrO_6. *Phys. Rev. Lett.* **109**, 157401 (2012).
34. G. Cao *et al.*, Novel magnetism of Ir^{5+} ($5d^4$) ions in the double perovskite Sr_2YIrO_6. *Phys. Rev. Lett.* **112**, 056402 (2014).
35. J. Liu *et al.*, Quantum confinement of Mott electrons in ultrathin $LaNiO_3/LaAlO_3$ superlattices. *Phys. Rev. B* **83**, 161102(R) (2011).
36. R. Morrow *et al.*, Magnetism in Ca_2CoOsO_6 and Ca_2NiOsO_6: Unraveling the mystery of superexchange interactions between 3d and 5d ions. *Chem. Mater.* **28**, 3666–3675 (2016).
37. J. Chakhalian *et al.*, Asymmetric orbital-lattice interactions in ultrathin correlated oxide films. *Phys. Rev. Lett.* **107**, 116805 (2011).
38. X. Liu *et al.*, Synthesis and electronic properties of Ruddlesden-Popper strontium iridate epitaxial thin films stabilized by control of growth kinetics. *Phys. Rev. Mater.* **1**, 075004 (2017).
39. M. A. Laguna-Marco *et al.*, Electronic structure, local magnetism, and spin-orbit effects of Ir(IV)-, Ir(V)-, and Ir(VI)-based compounds. *Phys. Rev. B* **91**, 214433 (2015).
40. D. Doennig, W. E. Pickett, R. Pentcheva, Confinement-driven transition between topological and Mott phases in $(LaNiO_3)_N/(LaAlO_3)_M$ (111) superlattices. *Phys. Rev. B* **89**, 121110(R) (2014).
41. J. Chaloupka, G. Khaliullin, Orbital order and possible superconductivity in $LaNiO_3/LaMO_3$ superlattices. *Phys. Rev. Lett.* **100**, 016404 (2008).

42. M. Wu *et al.*, Strain and composition dependence of orbital polarization in nickel oxide superlattices. *Phys. Rev. B* **88**, 125124 (2013).
43. O. Peil, M. Ferrero, A. Georges, Orbital polarization in strained $LaNiO_3$: Structural distortions and correlation effects. *Phys. Rev. B* **90**, 045128 (2014).
44. D. Haskel *et al.*, Pressure tuning of the spin-orbit coupled ground state in Sr_2IrO_4. *Phys. Rev. Lett.* **109**, 027204 (2012).
45. S. Fujiyama *et al.*, Spin and orbital contributions to magnetically ordered moments in 5d layered perovskite Sr_2IrO_4. *Phys. Rev. Lett.* **112**, 016405 (2014).
46. J.-W. Kim *et al.*, Controlling entangled spin-orbit coupling of 5d states with interfacial heterostructure engineering. *Phys. Rev. B* **97**, 094426 (2018).
47. F. Zuo *et al.*, Habituation based synaptic plasticity and organismic learning in a quantum perovskite. *Nat. Commun.* **8**, 240 (2017).
48. Y. Sun *et al.*, Strongly correlated perovskite lithium ion shuttles. *Proc. Natl. Acad. Sci. U.S.A.* **115**, 9672–9677 (2018).
49. Z. Radović, N. Božović, I. Božović, Photoinduced expansion of cuprate superconductors: Evidence of strong electron-lattice coupling. *Phys. Rev. B* **77**, 092508 (2008).
50. T. Oka, N. Nagaosa, Interfaces of correlated electron systems: Proposed mechanism for colossal electroresistance. *Phys. Rev. Lett.* **95**, 266403 (2005).
51. M. Kareev *et al.*, Sub-monolayer nucleation and growth of complex oxides at high supersaturation and rapid flux modulation. *J. Appl. Phys.* **109**, 114303 (2011).
52. G. Kresse, J. Furthmüller, Efficient iterative schemes for *ab initio* total-energy calculations using a plane-wave basis set. *Phys. Rev. B* **54**, 11169–11186 (1996).
53. J. P. Perdew, K. Burke, M. Ernzerhof, Generalized gradient approximation made simple. *Phys. Rev. Lett.* **77**, 3865–3868 (1996).
54. J. P. Perdew, K. Burke, M. Ernzerhof, Generalized gradient approximation made simple. *Phys. Rev. Lett.* **77**, 3865 (1996).
55. P. E. Blöchl, Projector augmented-wave method. *Phys. Rev. B* **50**, 17953–17979 (1994).
56. G. Kresse, D. Joubert, From ultrasoft pseudopotentials to the projector augmented-wave method. *Phys. Rev. B* **59**, 1758–1775 (1999).
57. A. Liechtenstein, V. Anisimov, J. Zaanen, Density-functional theory and strong interactions: Orbital ordering in Mott-Hubbard insulators. *Phys. Rev. B* **52**, R5467– R5470 (1995).
58. P. E. Blöchl, O. Jepsen, O. K. Andersen, Improved tetrahedron method for Brillouin-zone integrations. *Phys. Rev. B* **49**, 16223–16233 (1994).